Editors' Suggestion

# Transient response of a gain-driven polariton

Y.S. Gui* and C.-M. Hu

*Department of Physics and Astronomy, University of Manitoba, Winnipeg R3T 2N2, Canada*

(Received 29 August 2023; revised 11 March 2024; accepted 26 March 2024; published 12 April 2024)

We explore the transient response of a gain-embedded cavity magnon polariton system using time-domain measurements. The intricate interplay of gain, loss, and the light-matter interaction gives rise to distinctive dynamic behaviors, which can be categorized as damping, zero damping, and antidamping. The antidamping state triggers a unique exponential decay process, with the decay rate experiencing exponential amplification over time. This dynamic behavior results in an exceptionally swift decline in polariton amplitude, exceeding the pace of conventional constant-exponential decay processes. These findings have significant implications for advancing polariton devices, facilitating the rapid initiation of monochromatic microwave and light emission, and amplification in pulsed-mode operation.

DOI: 10.1103/PhysRevApplied.21.044023

## I. INTRODUCTION

The strong coupling between magnetic materials and microwave cavities has recently attracted significant attention due to its promising applications in classical and quantum computing [1–3]. This intriguing phenomenon gives rise to cavity magnon polaritons (CMPs) [4], which can be seen as hybrid states that possess both photonic and magnonic characteristics [5–10]. CMPs not only serve as a remarkable demonstration of their composite nature, combining the properties of photons and spins, but they also unlock a range of insights and functionalities that are inaccessible in the individual, uncoupled subsystems. These include advancements in cavity spintronics [10–12], quantum magnonics [13,14], memory architectures [15,16], polariton bistabilities [17], exceptional points [18,19], level attraction [20,21], unidirectional invisibility [22], singularity [23], and Floquet cavity electromagnonics [24].

Similar to classical oscillatory systems, the polariton's lifetime is inversely proportional to its damping rate. In the specific context of a pure coherent coupled linear system, this damping rate is determined by the linear superposition of damping rates originating from its light and matter components, consequently placing a constraint on the polariton's lifetime [25,26]. In a recent study, researchers harnessed a gain-embedded cavity magnonics platform to engineer a gain-driven polariton (GDP) [27]. This nonlinear system displays distinctive dynamics, including polariton auto-oscillations and self-selection of a bright mode—characterized by a sustained oscillation, as opposed to a dark mode that fades away within a limited time. Analogous to lasers and masers [28–30], GDP emission demonstrates features, such as injection locking and frequency-comb generation, holding the potential to serve as a high-quality coherent microwave source and offer polariton-based microwave amplification. However, the intricate dynamics behind the generation of dark and bright GDP modes, along with their associated time scales, fall outside the purview of steady-state behavior [27]. This constrains the GDP's appropriateness for pulse-mode operation and its capacity to promptly deliver the necessary low-noise emission and amplification.

In this paper, we present the transient behavior of the GDP, highlighting the cooperative impact of gain, loss, and coupling on the generation dynamics of the bright and dark GDP modes. Notably, the emergence of an antidamping GDP state triggers a distinctive exponential decay process, where the decay rate undergoes exponential amplification over time. This dynamic behavior results in an exceptionally swift decline in polariton amplitude, breaking the constraints imposed by the conventional constant-exponential decay process.

## II. NUMERICAL SIMULATION OF TRANSIENT RESPONSE

To gain insights into the transient response of the GDP, we begin by examining a simplified scenario governed by pure coherent coupling, $J$, expressed as

$$\dot{a} = -i\tilde{\omega}_a a - iJm, \tag{1a}$$

$$\dot{m} = -i\tilde{\omega}_m m - iJa. \tag{1b}$$

In this equation, $a$ and $m$ are scalar complex numbers representing the expected values of $\hat{a}$ and $\hat{m}$ operators for

*Corresponding author: ysgui@physics.umanitoba.ca

 

the cavity's and magnon's coherent states, respectively. The complex frequency of the magnon mode is represented as $\tilde{\omega}_m = \omega_m - i\kappa_m$, with $\kappa_m$ indicating its damping rate. The cavity's complex frequency, represented by $\tilde{\omega}_a = \omega_a + i(G - \kappa_a - \gamma|a|^2)$, consists of two extra components in addition to the linear cavity damping rate $\kappa_a$: the one-photon gain $G$ and the two-photon absorption $\gamma|a|^2$ [31,32], serving as quantum counterparts to negative damping and nonlinear damping in a van der Pol oscillator [33]. Maintaining equilibrium between the gain and loss, the steady-state amplitude of the uncoupled cavity is denoted as $A_c = \sqrt{(G - \kappa_a)/\gamma}$.

Simulated transient response of Eq. (1) are presented in Figs. 1(a) and 1(b), where the beat pattern of $m(t)$ diminishes due to the superposition of the time-decaying dark mode and the time-independent bright mode. The presence of these modes is identified through fast Fourier transform (FFT) analysis in Fig. 1(c). Their frequencies roughly align with the CMP eigenfrequencies, expressed as $\tilde{\omega}_\pm = \omega_\pm - i\delta\omega_\pm = (\tilde{\omega}_m + \tilde{\omega}_a)/2 \pm \sqrt{(\tilde{\omega}_m - \tilde{\omega}_a)^2/4 + J^2}$. The decay

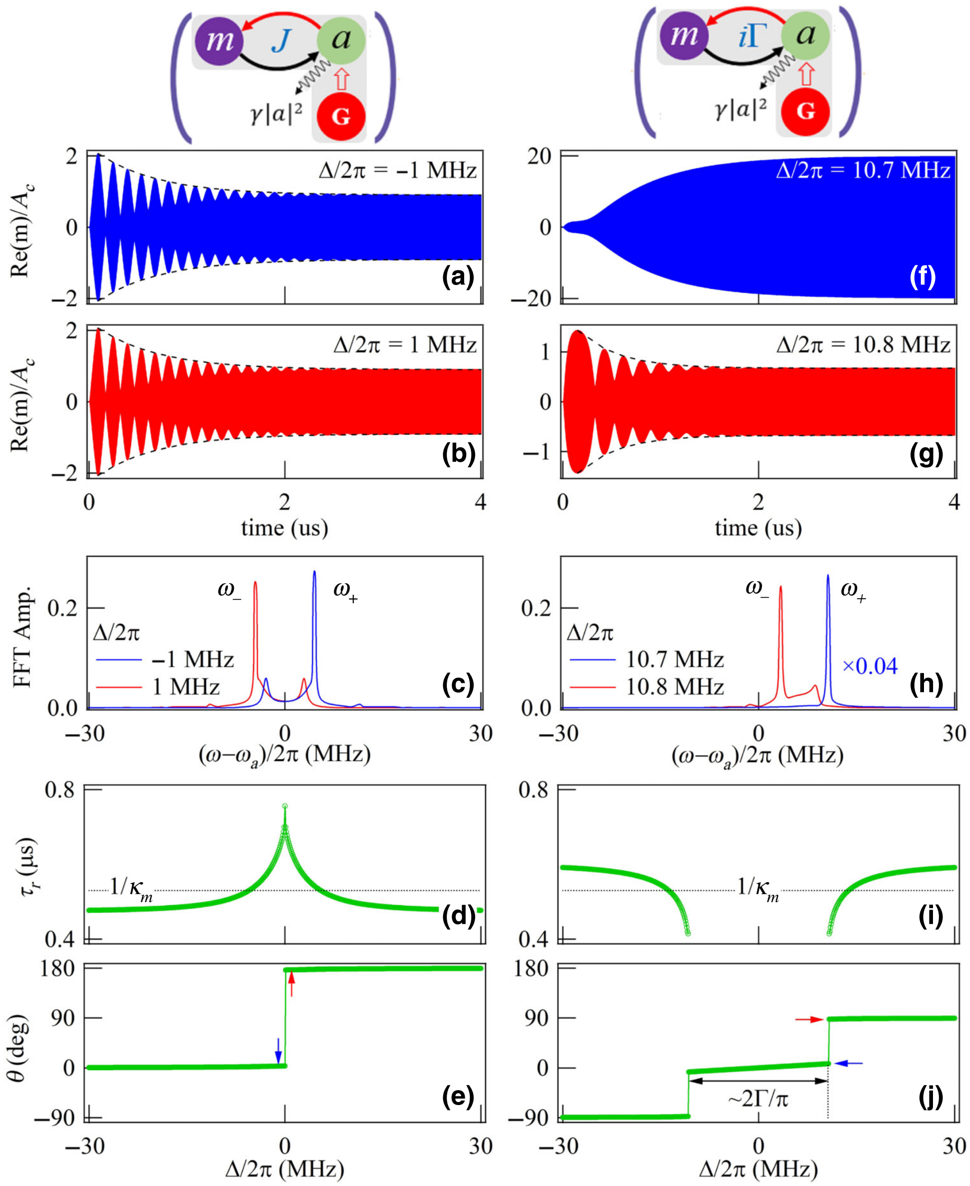


FIG. 1. Transient dynamics of coupled GDP systems. Numerical simulations using Eq. (1) with parameters $(G - \kappa_a)/2\pi$, $\kappa_m/2\pi$, and $J/2\pi = 170, 0.3$, and 5 MHz, respectively. The initial conditions were set as $a(0) \sim 0$ and $m(0) \sim 0$. Time evolution of Re$[m(t)]$ near the critical detuning at $\Delta/2\pi$ = (a) −1 MHz and (b) 1 MHz, with dashed lines indicating the exponential decay of the beating pattern. (c) FFT spectra of Re$(m)$. (d) Relaxation time of the dark GDP mode, with the dashed line indicating the magnon mode lifetime, $1/\kappa_m$. (e) Relative phase $\theta$ between $a$ and $m$ of the steady GDP state as a function of detuning $\Delta = \omega_m - \omega_a$. Similar arrangement for (f)–(j) simulated with $\Gamma/2\pi = 5$ MHz.

in Figs. 1(a) and 1(b) is governed by dashed lines, demonstrating a proportional relationship to $\exp(-t/\tau_r)$, where $\tau_r$ represents the relaxation time governing the decay of the dark GDP mode. This dynamic process is reminiscent of a damped-driven oscillator referring to Appendix A, where the magnon is compelled to oscillate at the driving frequency under external forcing.

In Fig. 1(d), the relaxation time $\tau_r$ peaks at the critical detuning $\Delta_c = 0$, aligned with the phase singularity [27] depicted in Fig. 1(e). The saturation of $\tau_r \sim 1/\kappa_m$, highlights the significant impact of magnon lifetime on the transient response of the GDP. Notably, yttrium iron garnet (YIG) features an ultranarrow linewidth (down to 45 kHz [34]), corresponding to a remarkable 4-μs lifetime.

Next, we investigate the transient response of a pure dissipative coupled GDP system. Within a specific range, a phenomenon known as mode locking or phase locking takes place [35–37]. In this regime, the polariton frequencies $\omega_\pm$ coalesce, giving rise to a unified FFT peak [blue curve in Fig. 1(h)]. Here, the dissipative coupling functions as an effective gain, promoting in-phase motion between $a$ and $m$. Conversely, it impedes polariton motion when $a$ and $m$ are in antiphase motion. In the in-phase motion, the initial exponential increase in the amplitudes of $a$ and $m$ is soon counteracted by the significant contribution from nonlinear damping, $\gamma|a|^2$. Consequently, the dynamic process to produce a stable GDP state is considerably slower than the exponential growth as shown in Fig. 1(f).

Beyond the phase-locking range, the dark mode exhibits a distinct frequency from the bright mode. Following a few microseconds relaxation [Fig. 1(g)], the system undergoes monochromatic polariton emission. The observed reduction in relaxation time $\tau_r$, as depicted in Fig. 1(i), occurs as the system approaches the phase singularity, contrasting with the behavior seen in coherent coupling. This discrepancy is linked to the typical feature of linewidth repulsion, in contrast to the linewidth attraction observed in coherent coupling [26].

## III. EXPERIMENTAL RESULTS AND DISCUSSION

In this section, the subsequent experiment illustrates the acceleration of the conventional exponential decay process. Here, the self-sustaining cavity used is a half-wavelength microstrip line resonator mutually coupled to two measurement ports. The magnetic sample is a 1-mm diameter YIG sphere positioned near the coupling port. The calibrated device parameters include $G/2\pi = 312$, $\kappa_a/2\pi = 142$, $\gamma/2\pi = 2.6 \times 10^{-12}$ MHz, and $\omega_a/2\pi = 3.587$ GHz. The Kittel mode frequency, $\omega_m$, is controlled by a magnetic field, and its damping rate is $\kappa_m/2\pi = 0.8$ MHz.

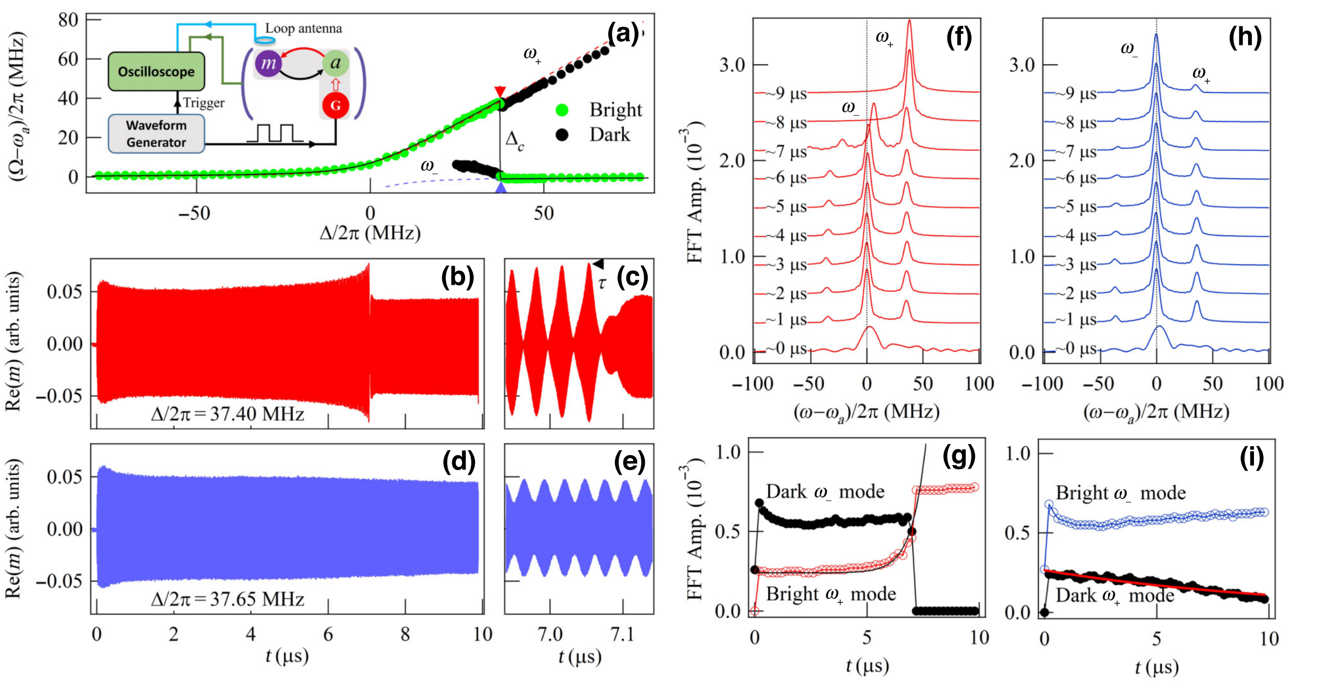


FIG. 2. Damped versus antidamped GDP states. (a) Measured frequencies for bright (green symbols) and dark (black symbols) GDP modes. Solid line: simulated dispersion of bright GDP mode; dashed lines: CMP dispersion. Inset: schematic of experimental setup capturing cavity and magnon dynamics with a high-speed real-time oscilloscope. (b),(d) Raw experimental data with enlarged pictures (c),(e). (f),(h) Typical FFT spectra (vertically offset for clarity) at different times for $\Delta < \Delta_c$ (red) and $\Delta > \Delta_c$ (blue), respectively. (g),(i) show amplitude evolution for bright and dark GDP modes, with black and red solid lines indicating exponential growth/decay curves.

A voltage pulse train is used to control the ON-OFF state of the gain. Transient microwave signals are efficiently captured through the utilization of a high-speed oscilloscope with a 33-GHz analogue bandwidth and a sampling rate of 100 GS/s. In addition to cavity dynamics, local magnon dynamics are detected using a small loop antenna.

Figure 2(a) displays the GDP frequencies of the bright (green symbols) and dark (black symbols) modes obtained from time-domain measurements. Notably, these frequencies exhibit a sudden switch at a critical detuning $\Delta_c/2\pi = 37.5$ MHz. To understand the experimental observation, we utilize a phenomenological model that replaces the coupling term $J$ in Eq. (1) with a complex coupling strength $J + i\Gamma$. By adjusting the parameters $J/2\pi = 7.8$ MHz and $\Gamma/2\pi = 4.1$ MHz, the numerical simulation replicates the dispersion of the bright GDP, as depicted by the solid line in Fig. 2(a).

In Figs. 2(b) and 2(d), we present the raw experimental data Re$(m)$ to emphasize the distinct dynamics observed across various detuning ranges. In the case of $\Delta > \Delta_c$ as illustrated in Fig. 2(d), the beating pattern gradually diminishes, similar to the observations discussed earlier in Fig. 1. Conversely, for $\Delta < \Delta_c$, the beating pattern in Fig. 2(b) initially experiences a gradual increase; however, at a critical time ($t \sim \tau$), it instantaneously evolves into a single-frequency oscillation within approximately 50 ns—orders of magnitude shorter than the time scale associated with exponential decay. This unique feature becomes more apparent in the magnified view presented in Fig. 2(c), defying conventional expectations.

The detailed temporal evolution of bright and dark GDP modes is analyzed using time-resolved FFT, as illustrated in Figs. 2(f)–2(i). As anticipated, the predominant motion components arise from the two polariton modes, with a frequency $\omega_-$ and $\omega_+$, respectively. This observation enables us to express the motion of the cavity and magnon as $a(t) = A_+(t)e^{-i\omega_+ t} + A_-(t)e^{-i\omega_- t}$ and $m(t) = M_+(t)e^{-i\omega_+ t} + M_-(t)e^{-i\omega_- t}$. Focusing on the $\omega_+$ mode, we observe amplification when $\Delta < \Delta_c$ and decay when $\Delta > \Delta_c$, resulting in a negative damping rate of $\delta\omega_+/2\pi = -0.26$ MHz and a positive damping rate of $\delta\omega_+/2\pi = 0.014$ MHz for these respective cases, as dictated by the exponential relation $A_+(t), M_+(t) \propto \exp(-\delta\omega_+ t)$.

Despite the frequency difference, the nonlinear damping term $\gamma|a|^2$ establishes a connection to the dynamic interaction between the two polariton modes. Specifically, the nonlinear damping terms for $\omega_-$ and $\omega_+$ modes can be computed as $\gamma(A_-^2 + 2A_+^2)$ and $\gamma(A_+^2 + 2A_-^2)$, respectively. Because the time required to reach a quasistable cavity state is orders of magnitude shorter than other dynamic processes, we can consider the magnonlike $\omega_+$ mode initially as a perturbation of the cavitylike $\omega_-$ mode, with $|A_+| \ll |A_-| \sim A_c$. Figures 2(g) and 2(i) confirm its validity, showing that the initial amplitude of $\omega_-$ mode dominates and remains unchanged despite different subsequent dynamics. In Appendix F, Fig. 7 provides a more straightforward comparison between these two cases.

Utilizing the perturbation induced by $A_+(t)$, we can obtain the motion equation for the $\omega_-$ mode:

$$\dot{A}_-(t) \approx -2\gamma A_+^2(t)A_-(t) \propto -\exp(-2\delta\omega_+ t)A_-(t). \quad (2)$$

As $A_+$ experiences exponential decay for $\Delta > \Delta_c$, the influence of the $\omega_+$ mode on the $\omega_-$ mode diminishes over time, resulting in a stabilized $A_-$ at a finite value. This dynamic process provides insight into the emergence of a bright cavitylike $\omega_-$ mode, achieved through a conventional exponential decay process of $\omega_+$ mode. In contrast, $\delta\omega_+ < 0$ when $\Delta < \Delta_c$, the decay rate in Eq. (2) exhibits exponential growth over time, leading to an exceptional decay process that far surpasses conventional exponential decay. In this case, the entire dynamic process of achieving stable monochromatic GDP emission is primarily determined by the time required to elevate $A_+$ to a level comparable to a fraction of $A_-$, such as $A_+ \sim A_-/2$, as

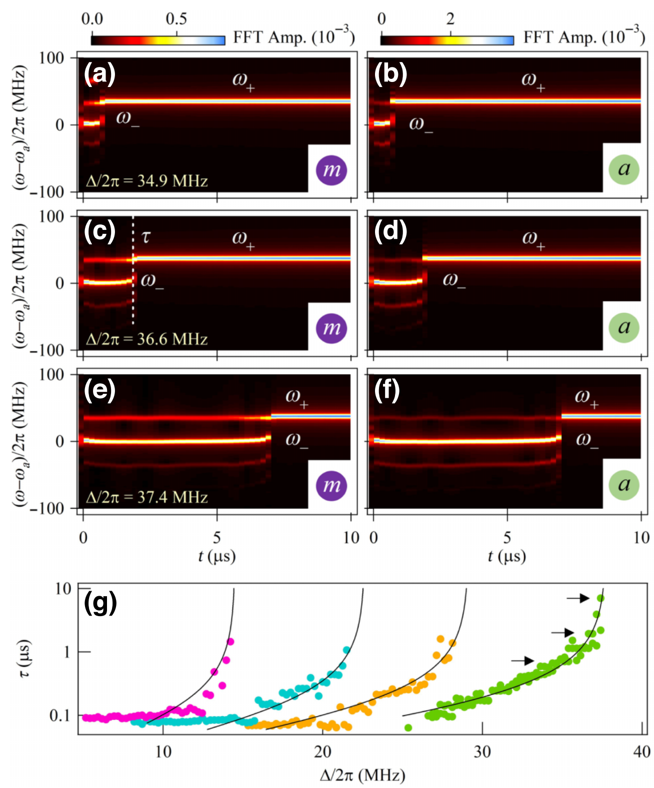


FIG. 3. GDP lifetime $\tau$. FFT amplitude mapping of Re$(m)$ in (a),(c),(e) and Re$(a)$ in (b),(d),(f) is shown over frequency and time for three detuning values. (g) Lifetime $\tau$ versus detuning under different coupling strengths. Solid lines guide rapid growth per our model. Green symbols correspond to Fig. 2 findings, and detailed parameters for other conditions are in Table I in Appendix E.

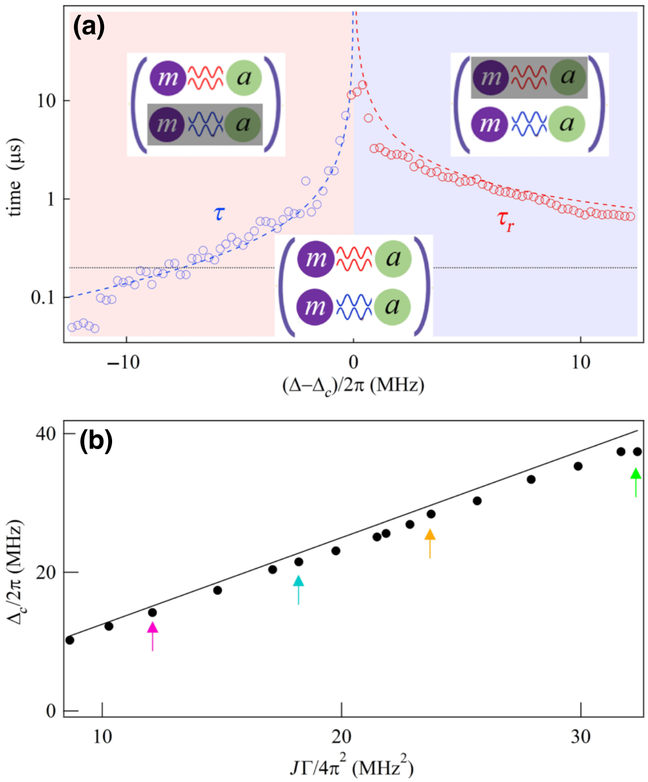


FIG. 4. Dynamic divergence and critical detuning. (a) Lifetime of dark $\omega_-$ mode lifetime (blue symbols) and relaxation time of dark $\omega_+$ mode (red symbols) as a function of detuning. Two dynamic ranges are separated by critical detuning $\Delta = \Delta_c$. Blue dashed curve approximates $\tau \propto -1/\delta\omega_+$, red dashed curve is the calculated relaxation time ($\tau_r = 1/\delta\omega_+$), and black dotted line represents magnon lifetime $1/\kappa_m$. (b) Measured critical detuning (solid symbols) versus the product of coupling strengths compared with estimated value (solid line). Color arrows indicate measurement in Fig. 3(g).

illustrated in Fig. 8 in Appendix G. Consequently, the lifetime of the dark $\omega_-$ mode, $\tau$, is inversely proportional to $-\delta\omega_+$.

The abrupt disappearance of the dark GDP mode is a frequently observed phenomenon, apparent across a wide range of detuning values and coupling strengths, as depicted in Fig. 3. The mappings, distinguished by the FFT amplitude, reveal that the initial influence of the $\omega_+$ mode is minimal, especially on the cavity motion. As time advances towards $\tau$, the amplitude of the $\omega_+$ mode gradually increases. After surpassing this duration, the amplitude of the $\omega_-$ mode experiences a sudden and complete extinguishment, leading to the swift establishment of a stable monochromatic GDP emission.

These results also visually demonstrate the impact of detuning on the lifetime. In Fig. 3(g), where the experimentally obtained lifetimes $\tau$ (depicted by symbols) are presented as a function of detuning for four distinct cases with varying coupling strengths. The plot unveils a divergence phenomenon as the detuning parameter $\Delta$ approaches a critical value $\Delta_c$. Here the lifetime $\tau$ experiences a rapid increase, transitioning from less than 100 ns to around 10 μs—a substantial growth spanning 2 orders of magnitude.

To deepen our understanding of the divergence effect from a dynamic perspective, Fig. 4(a) illustrates the lifetime, $\tau$, of the dark $\omega_-$ mode (depicted in blue) and the relaxation time, $\tau_r$, of the dark $\omega_+$ mode (depicted in red) as functions of detuning. Note that $\tau$ represents the true lifetime of the dark mode, denoting the point when the mode amplitude is entirely extinguished, while $\tau_r$ indicates the time for its amplitude to decay to $1/e$. Despite differing dynamics, both $\tau$ and $\tau_r$ exhibit divergence as $\Delta$ approaches $\Delta_c$. At the critical condition $\Delta = \Delta_c$, both polariton modes are in a stable state, $\delta\omega_+ = \delta\omega_- = 0$, showing neither decay nor growth. This characteristic extends beyond discussions in Fig. 1, as in these cases, $\tau_r$ maintains a finite value as shown in Figs. 1(d) and 1(i).

Finally, the experimental observed critical detuning (depicted by symbols) is shown in Fig. 4(b) as a function of the product of coupling strengths. In consideration of the perturbation approximation outlined in Appendix B, it is suggested that the initial damping rate of the $\omega_+$ mode can be described as,

$$\delta\omega_+ = \kappa_m - J\Gamma/\Delta. \tag{3}$$

As a result, this relation yields an estimated critical detuning, indicated by a solid line in Fig. 4(b), where $\delta\omega_+ = 0$. By varying the detuning, the $\omega_+$ modes undergo a transition from antidamping to damping states.

## IV. CONCLUSIONS

In summary, our study has offered a comprehensive analysis of the transient response exhibited by a GDP device that incorporates gain and light-matter interaction. Our findings illuminate the interplay among gain, loss, and coupling gives rise to a diverse range of polariton dynamics. This manipulation results in the emergence of distinctive polariton states characterized by damping, zero damping, and antidamping properties. Notably, the antidamping state induces a rapid decay of the GDP dark mode, with the decay rate exponentially amplifying over time. Such an acceleration in the start-up process holds intriguing possibilities for advancing the development of ultrafast polariton devices dedicated for coherent light emission and amplification at various frequency bands.

## ACKNOWLEDGMENTS

This work has been funded by NSERC Discovery Grants and NSERC Discovery Accelerator Supplements (C.-M.H.). We thank B. Yao, J.W. Rao, M. Kim, and

G. Kozyniak for their valuable contributions in fabricating various test devices. In additionally, we acknowledge CMC Microsystems for providing equipment that facilitated this research.

## APPENDIX A: DAMPED-DRIVEN OSCILLATOR

A damped-driven magnon mode can be described by the equations of motion

$$\dot{a} = -i\tilde{\omega}_a a, \tag{A1a}$$

$$\dot{m} = -i\tilde{\omega}_m m - iJa, \tag{A1b}$$

in a unidirectional coupling scheme. The complex frequency of the magnon mode is represented by $\tilde{\omega}_m = \omega_m - i\kappa_m$, where $\kappa_m$ denotes the total magnon damping rate. Additionally, the coupling strength between cavity photons and magnons is denoted by $J$.

The complex eigenfrequencies of the system are $\tilde{\omega}_a$ and $\tilde{\omega}_m$, with their corresponding eigenvectors represented by $\vec{p}_b = \begin{bmatrix} -(\Delta - i\kappa_m)/J \\ 1 \end{bmatrix} \begin{bmatrix} a \\ m \end{bmatrix}$ and $\vec{p}_d = \begin{bmatrix} 0 \\ 1 \end{bmatrix} \begin{bmatrix} a \\ m \end{bmatrix}$, respectively. Here, $\Delta = \omega_m - \omega_a$ is frequency detuning between the magnon and cavity modes.

To explain the reasons why $\vec{p}_b$ is associated with the bright mode, whereas $\vec{p}_d$ is associated with the dark mode, let us neglect the rapid start-up of the cavity motion by assuming $a(t) = A_c e^{-i\omega_a t}$. Then the magnon motion can be analytically solved according to Eq. (A1b), expressed as

$$m(t) = \frac{e^{-i\omega_a t} - e^{-\kappa_m t - i\omega_m t}}{-\Delta + i\kappa_m} A_c J. \tag{A2}$$

This equation explicitly demonstrates how the magnon damping rate controls the time needed to generate monochromatic oscillations. Here, the relaxation process of the dark mode can be described by an exponential decay function, $\propto e^{-t/\tau_r}$, with $\tau_r = \tau_m = 1/\kappa_m$, where $\tau_m$ denotes the magnon lifetime. In addition, Eq. (A2) also anticipates that the relative phase, $\theta$, between $a$ and $m$ for the bright mode rapidly transitions from 0 to 180° near $\Delta = 0$.

## APPENDIX B: DAMPED AND ANTIDAMPED POLARITON STATES

In this section, we go through how the bright and dark GDP modes form dynamically. We focus on the dynamic process that occurs after the amplitude of the active cavity (a van der Pol oscillator) reaches saturation, which takes about 10 ns for $G/2\pi > 100$ MHz. After this time, the solution of the following motion equations:

$$\dot{a} = -i\tilde{\omega}_a a - i(J + i\Gamma)m, \tag{B1a}$$

$$\dot{m} = -i\tilde{\omega}_m m - i(J + i\Gamma)a, \tag{B1b}$$

may have a form of

$$a(t) = A_-(t)\exp(-i\omega_- t) + A_+(t)\exp(-i\omega_+ t), \tag{B2a}$$

$$m(t) = M_-(t)\exp(-i\omega_- t) + M_+(t)\exp(-i\omega_+ t), \tag{B2b}$$

which separates the fast oscillation from other slow motion in $A_\pm$ and $M_\pm$.

The interaction between the two GDP modes is manifested through the nonlinear damping term $\gamma|a|^2$. Defining real values for $A_-$ and $A_+$ for simplicity, a simple relation is established

$$|a|^2 = A_-^2 + A_+^2 + 2A_-A_+\cos[(\omega_- - \omega_+)t]. \tag{B3}$$

By applying Euler's formula for cosine, $\cos x = (e^{ix} + e^{-ix})/2$, and decomposing the terms associated with frequencies $\omega_-$ and $\omega_+$ terms, the nonlinear damping terms for the $\omega_-$ and $\omega_+$ modes can be expressed as $\gamma(A_-^2 + 2A_+^2)$ and $\gamma(A_+^2 + 2A_-^2)$, respectively. This analysis provides a clear understanding of the specific contribution of nonlinear damping effects from both modes.

To elucidate the fundamental physics without relying on complex mathematics, we examine the scenario where $J^2 \gg \Gamma^2$ and $\Delta > 0$. We can assign $\omega_-$ (approximately $\omega_a$, when $\Delta^2 \gg J^2$) to represent the antiphase cavitylike mode and $\omega_+$ (approximately $\omega_m$, when $\Delta^2 \gg J^2$) to denote the in-phase magnonlike mode. Under these conditions, both $A_\pm$ and $M_\pm$ can be described as real numbers. For in-phase motion, dissipative coupling acts as an effective gain, facilitating the motion. Conversely, for antiphase motion, dissipative coupling serves as a highly efficient damping mechanism, hindering the motion.

With these considerations in mind, we initially investigate the cavitylike mode by substituting Eq. (B2) into cavity motion Eq. (B1a). Splitting the real and imaginary parts oscillating with a frequency $\omega_-$, we have

$$[G - \kappa_a - \gamma A_-^2(t) - 2\gamma A_+^2(t)]A_-(t) + \Gamma M_-(t) = \dot{A}_-(t), \tag{B4a}$$

$$(\omega_- - \omega_a)A_-(t) - JM_-(t) = 0. \tag{B4b}$$

Near $t = 0$, the system should satisfy the condition $|A_+| \ll |A_-| \sim A_c$, since the cavity amplitude saturates several orders of magnitude faster than other dynamic processes. Combining Eqs. (B4a) and (B4b), we obtain

$$\dot{A}_-(t) \approx \left[G - \kappa_a - \gamma A_-^2(t) + \frac{\Gamma}{J}(\omega_- - \omega_a)\right]A_-(t) \sim 0. \tag{B5}$$

Therefore, the solution of the cavitylike mode is

$$A_-(t) \sim A_c, \tag{B6a}$$

$$M_-(t) \sim \frac{\omega_- - \omega_a}{J} A_c. \tag{B6b}$$

This analysis indicates that the cavitylike $\omega_-$ mode initially manifests as a bright mode when the condition $|A_+/A_-| \ll 1$ is satisfied. It is noteworthy that $\omega_- < \omega_a$, resulting in the anticipated antiphase motion of $a$ and $m$ in the $\omega_-$ mode.

We then exam the motion of the magnonlike mode by substituting Eq. (B2) into Eq. (B1b) and splitting the real and imaginary parts oscillating with a frequency $\omega_+$. We can obtain

$$[G - \kappa_a - \gamma A_+^2(t) - 2\gamma A_-^2(t)]A_+(t) + \Gamma M_+(t) = \dot{A}_+(t), \tag{B7a}$$

$$(\omega_+ - \omega_a)A_+(t) - JM_+(t) = 0. \tag{B7b}$$

Given that $|A_+/A_-| \ll 1$, even a minor alteration in $A_-$ can induce a substantial fluctuation in $A_+$. Under these circumstances, the approximation as we did for the $\omega_-$ mode, is impractical for $\omega_+$ mode. Here, it is necessary to establish two additional relationships by substituting Eq. (B2) into Eq. (B1b)

$$-\kappa_m M_+(t) + \Gamma A_+(t) = \dot{M}_+(t), \tag{B8a}$$

$$(\omega_+ - \omega_m)M_+(t) - JA_+(t) = 0. \tag{B8b}$$

To clarify the impact of detuning, $\Delta$, it is necessary to combine Eqs. (B7b) and (B8a), which yields the relation

$$\dot{M}_+(t) = \left(-\kappa_m + \frac{\Gamma J}{\omega_+ - \omega_a}\right) M_+(t), \tag{B9}$$

and its solution is

$$\begin{aligned} M_+(t) &= M_+(t_0) \exp\left[\left(-\kappa_m + \frac{\Gamma J}{\omega_+ - \omega_a}\right)(t - t_0)\right] \\ &\approx M_+(t_0) \exp\left[\left(-\kappa_m + \frac{\Gamma J}{\Delta}\right)(t - t_0)\right]. \end{aligned} \tag{B10}$$

Substituting it into Eq. (B7b), we obtain

$$A_+(t) \approx \frac{JM_+(t_0)}{\Delta} \exp\left[\left(-\kappa_m + \frac{\Gamma J}{\Delta}\right)(t - t_0)\right]. \tag{B11}$$

The above two equations indicates the effective damping rate of the $\omega_+$ mode,

$$\delta\omega_+ = \kappa_m - \frac{\Gamma J}{\Delta}. \tag{B12}$$

This equation is denoted as Eq. (3) in the main text. Depending on the detuning, this damping rate may manifest as either positive or negative, indicative of the damped or antidamped state, respectively. When the detuning reaches a critical point, the damping rate $\delta\omega_+$ becomes zero. In conjunction with Eq. (B6), where $\delta\omega_- = 0$, the amplitudes of both $\omega_+$ and $\omega_-$ modes neither decrease nor increase over time, indicating a simultaneous existence of two bright modes. This relation elucidates the physics behind the observed critical detuning in Fig. 2.

## APPENDIX C: RAPID DECAY PROCESS

When $\delta\omega_+ > 0$, the amplitude of $M_+$ and $A_+$ exponentially decays. Consequently, the condition $|A_+/A_-| \ll 1$ is maintained over time, leading to the emergence of bright cavitylike $\omega_-$ mode alongside the dark magnonlike $\omega_+$ mode. This phenomenon is essentially related to the behavior of damped driven oscillators as discussed in Appendix A.

However, if $\delta\omega_+ < 0$, the amplitude of $M_+$ and $A_+$ exponentially grows. Notably, this antidamped state is not sustainable for an extended duration because the condition $|A_+/A_-| \ll 1$ is violated. In this case, Eq. (B5) becomes

$$\dot{A}_-(t) \approx -2\gamma A_+^2(t) A_-(t). \tag{C1}$$

As the amplitude $A_+(t)$ experiences exponential growth over time with a rate of $-\delta\omega_+$, the approximate solution of $A_-(t)$ reveals a distinct form as

$$A_-(t) \propto \exp[C_0 \exp(-2\delta\omega_+ t)/\delta\omega_+], \tag{C2}$$

where $C_0 = \gamma J^2 M_+^2(t_0)/\Delta^2$ is a positive constant. Crucially, this expression emphasizes the rapid decay of amplitude $A_-$ when $\delta\omega_+ < 0$, which is characterized by an exceptionally swift decline of the amplitude of the cavitylike $\omega_-$ mode that far exceeds the traditional exponential decay. The evolving dynamics give rise to the emergence of the bright magnonlike $\omega_+$ mode (along with the dark cavitylike $\omega_-$ mode). This process effectively surpasses the constraints typically associated with magnon relaxation in damped-driven oscillators, facilitating a prompt initiation of monochromatic polariton emission.

Equation (C2) remains valid when $\delta\omega_+ > 0$. In this scenario, as $t$ approaches infinity, the term $\exp(-2\delta\omega_+ t)$ diminishes, driving $A_-(t \to +\infty)$ to stabilize at a constant value as described in Eq. (B6a).

## APPENDIX D: TIME-DOMAIN MEASUREMENT SETUP

A DS345 synthetic function generator from Stanford Research generates a square wave with a frequency of 20 kHz, which is utilized to control the gain's ON-OFF state. The rise time is less than 15 ns. The time-domain measurements were directly taken with a Tektronix DPO73304SX Digital Phosphor Oscilloscope with a 33-GHz analogue bandwidth and a sampling rate of 100 GS/s. We turn on the device at $t = 0$ and simultaneously record the temporal evolution of $a$ and $m$ between $t = -0.1$ and 9.9 μs, equal to 1 million data points. The cavity dynamics are

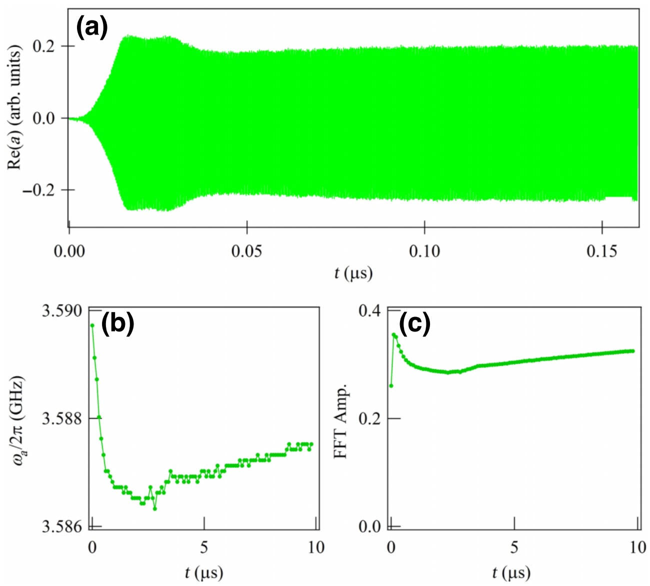


FIG. 5. (a) Start-up of the active cavity. The cavity frequency (b) and its corresponded FFT amplitude (c) as a function of time.

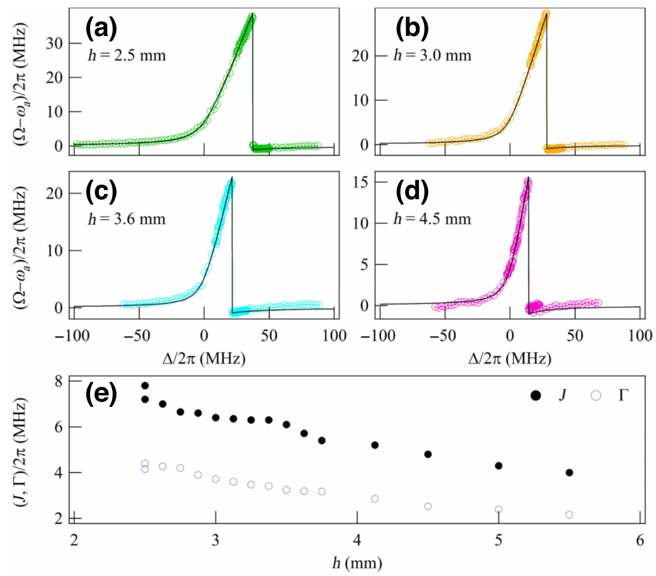


FIG. 6. (a)–(d) Measured (solid symbols) and simulated (solid lines) frequency of the bright GDP mode as a function of detuning at different height. The coupling strength used in the simulation is (a) $J/2\pi = 7.8$ MHz and $\Gamma/2\pi = 4.1$ MHz, (b) $J/2\pi = 6.4$ MHz and $\Gamma/2\pi = 3.7$ MHz, (c) $J/2\pi = 5.7$ MHz and $\Gamma/2\pi = 3.2$ MHz, and (d) $J/2\pi = 4.8$ MHz and $\Gamma/2\pi = 2.5$ MHz. (e) The deduced coherent coupling strength $J$ and dissipative coupling strength $\Gamma$ as a function of the YIG height $h$.

detected through a coaxial cable connected to the coupling port of the active cavity, while local magnon dynamics are observed using a small loop antenna with a diameter of approximately 2 mm mounted on top of the YIG sphere. The FFT analysis was then utilized to translate a microwave signal from the time domain to a frequency domain representation for analyzing the GDP frequency.

The active cavity is a half-wavelength microstrip line resonator whose width matches 50-Ω impedance. A voltage-controlled microwave amplifier (a bipolar junction transistor, BJT) is inserted to realize the gain. Reference [27] contains the detailed design of the active cavity as well as device calibration with $G/2\pi = 312$, $\kappa_a/2\pi = 142$, and $\gamma/2\pi = 2.6 \times 10^{-12}$ MHz. The transient behaviors of the cavity are now presented. Figure 5(a) depicts the cavity startup (at a detuning of $\Delta/2\pi \sim -100$ MHz), which takes roughly 20 ns in agreement with the simulation result, approximately 10 ns. The cavity frequency experiences an initial drop of around 3 MHz within the first microsecond before gradually stabilizing, as shown Fig. 5(b). This observation sheds light on the deviation of the dark cavitylike mode from the theoretical prediction when $\Delta < \Delta_c$ in Fig. 2(a). The decline in cavity frequency over time may be linked to thermal effects originating from a semiconductor BJT, especially given that the input power exceeds 100 mW [27].

## APPENDIX E: COUPLING STRENGTH CHARACTERIZATION

A 1-mm diameter YIG sphere is mounted on a probe attached to an $x$-$y$-$z$ stage, allowing its location to be precisely controlled with a 5-μm resolution. The damping rate of the magnon mode is calibrated as $\kappa_m/2\pi = 0.8$ MHz. The coupling strength was regulated in this study by adjusting the YIG height, $h$, to the substrate. Time-dependent FFT analysis was performed at 0.2-μs intervals, and the frequency of the bright GDP mode was read according to the position of the primary FFT peak at $t \sim 10$ μs. The typical dispersion of the bright GDP mode (solid symbols) is shown in Fig. 6. Numerical simulation (lines) based on Eq. (B1) is used to fit the experimental dispersion by adjusting the coupling strength $J$ and $\Gamma$. Unless stated otherwise, the experimental results are presented for $h = 2.5$ mm, where $J/2\pi = 7.8$ MHz and $\Gamma/2\pi = 4.1$ MHz.

Table I lists the coupling parameters used in Fig. 3 in the main text, where the fitting of lifetimes is based on Eq. (3) [as illustrated, for instance, in Fig. 9(h)].

TABLE I. Coupling parameters for Fig. 3 in the main text.

| | Dispersion Fitting | | Lifetime Fitting |
|---|---|---|---|
| Symbol color | $J/2\pi$ (MHz) | $\Gamma/2\pi$ (MHz) | $J\Gamma/4\pi^2$ (MHz$^2$) |
| Green | 7.8 | 4.1 | 30.3 |
| Orange | 6.4 | 3.7 | 23.3 |
| Cyan | 5.7 | 3.2 | 18.1 |
| Pink | 4.8 | 2.5 | 11.6 |

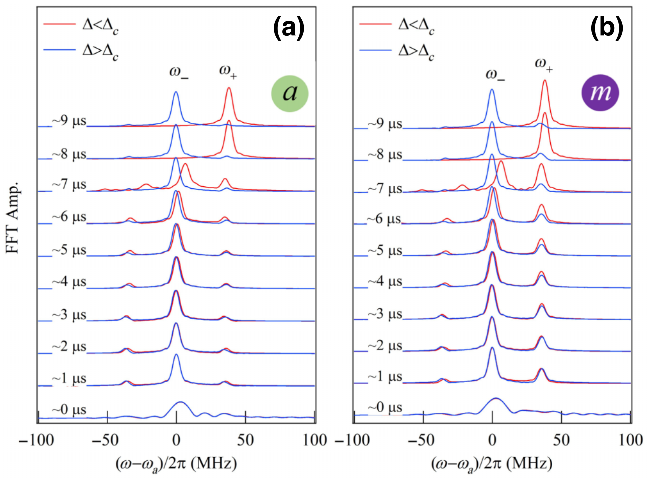


FIG. 7. Comparison of the temporal development of the GDP dynamics at $\Delta < \Delta_c$ ($\Delta/2\pi = 37.40$ MHz, red curves) and $\Delta > \Delta_c$ ($\Delta/2\pi = 37.65$ MHz, blue curves) using FFT analysis for (a) $a$ and (b) $m$. The curves are vertically offset for clarity.

## APPENDIX F: TIME-EVOLUTION COMPARISON BELOW AND ABOVE $\Delta_c$

Figures 7(a) and 7(b) compare the temporal development of the GDP dynamics at $\Delta < \Delta_c$ ($\Delta/2\pi = 37.40$ MHz, red curves) and $\Delta > \Delta_c$ ($\Delta/2\pi = 37.65$ MHz, blue curves) using FFT analysis for $a$ and $m$, respectively. The FFT spectra were carried out in a time period of 0.2 μs, for example, the time $t \sim 0$ indicates the FFT spectrum between $t = [-0.1, 0.1]$ μs. Initially, the spectra are almost identical for both $\Delta < \Delta_c$ and $\Delta > \Delta_c$. Beginning with $t \sim 1$ μs, the difference for $\omega_+$ mode becomes increasingly obvious as its amplitude grows for $\Delta < \Delta_c$ and drops for $\Delta > \Delta_c$. Meanwhile, there is no substantial difference for $\omega_-$ mode before $t \sim 4$ μs, when the frequency $\omega_-$ begins to shift toward $\omega_+$ for $\Delta < \Delta_c$ but not for $\Delta > \Delta_c$. Between $t \sim 7$ and 8 μs, a monochromatic emission at $\omega_+$ is rapidly produced for $\Delta < \Delta_c$.

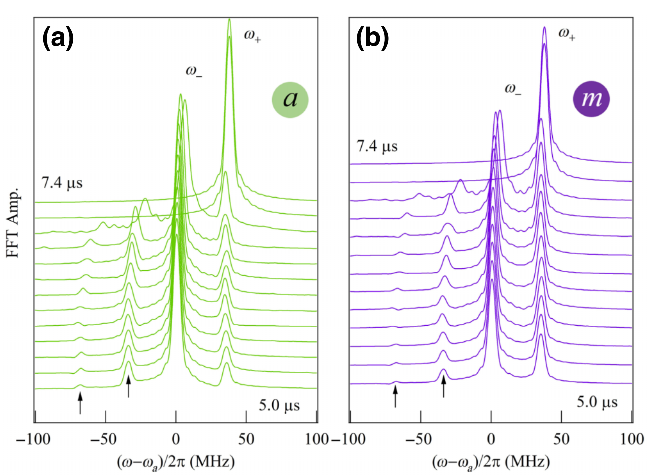


FIG. 8. Temporal development of the FFT spectrum at $\Delta < \Delta_c$ ($\Delta/2\pi = 37.40$ MHz) for (a) $a$ and (b) $m$ from $t = 5$ μs to $t = 7.4$ μs with a step of 0.2 μs. The lifetime of the dark $\omega_-$ mode is about $\tau \approx 7.05$ μs. The curves are vertically offset for clarity. Arrows indicate the sideband generation.

## APPENDIX G: FORMATION OF BRIGHT MAGNONLIKE GDP

The detailed dynamics for developing a magnonlike bright GDP are depicted in Fig. 8. In addition to the two polaritons, high-order sidebands are produced. When approaching the critical time $t = \tau \approx 7.05$ μs, the amplitude of the $\omega_+$ mode and the sideband grow. Meanwhile the frequencies of the $\omega_-$ mode and the sideband emission blueshift toward the $\omega_+$ mode, which emerges as the system's attractor. Between $t = 7.0$ and 7.2 μs, a stable condition is instantaneously established, and all other modes are absorbed by the $\omega_+$ mode, resulting in a system monochromatic oscillating at the frequency $\omega_+$.

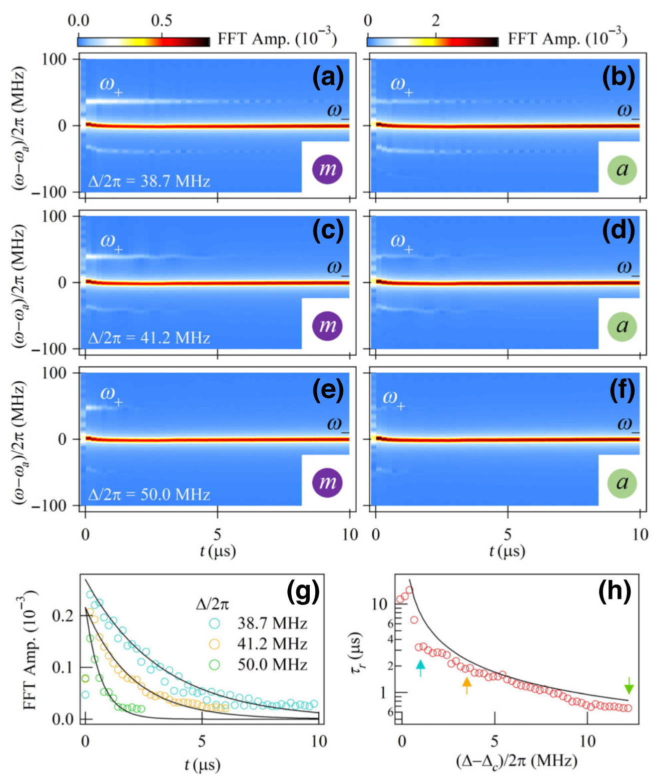


FIG. 9. FFT amplitude mapping of (a),(c),(e) Re($m$) and (b),(d),(f) Re($a$) as a function of frequency and detuning for $\Delta/2\pi = 38.7$, 41.2, and 50.0 MHz, respectively. (g) The FFT amplitude of the $\omega_+$ mode (symbols) as a function of time calculated from Re($m$), and the curves are exponential decay, $\propto e^{-t/\tau_r}$, used to deduce the relaxation time $\tau_r$. (h) $\tau_r$ as a function of detuning, and the solid line is the calculation $\tau_r = 1/(\kappa_m - J\Gamma/\Delta)$ with $J\Gamma/4\pi^2 = 30.3$ MHz$^2$.

## APPENDIX H: RELAXATION TIME $\tau_r$ FOR $\Delta > \Delta_c$

Figures 9(a)–9(f) present the FFT amplitude of Re($m$) and Re($a$) mapped as a function of frequency and time for three typical detuning frequencies $\Delta/2\pi = 38.7, 41.2$, and 50.0 MHz. The amplitude of $\omega_+$ mode for both the cavity motion $a$ and the magnon motion $m$ gradually decrease over time. Finally, a monochromatic GDP emission is produced.

The FFT amplitude of the $\omega_+$ mode (symbols) calculated from Re($m$) is plotted in Fig. 9(g) as a function of time and fitted with exponential decay, $\propto e^{-t/\tau_r}$, to deduce the relaxation time $\tau_r$. As detuning approaches $\Delta_c$, the relaxation time $\tau_r$ dramatically increases as summarized in Fig. 9(h). When integrating this result with the evolution of $\tau$ over detuning for $\Delta < \Delta_c$, a singularity feature becomes prominent, as illustrated in Fig. 4(a). The same effects have been observed across various coupling strengths.


[1] D. Lachance-Quirion, Y. Tabuchi, A. Gloppe, K. Usami, and Y. Nakamura, Hybrid quantum systems based on magnonics, Appl. Phys. Express **12**, 070101 (2019).

[2] A. A. Clerk, K. W. Lehnert, P. Bertet, J. R. Petta, and Y. Nakamura, Hybrid quantum systems with circuit quantum electrodynamics, Nat. Phys. **16**, 257 (2020).

[3] H. Y. Yuan, Y. Cao, A. Kamra, R. A. Duine, and P. Yan, Quantum magnonics: When magnon spintronics meets quantum information science, Phys. Rep. **965**, 1 (2022).

[4] B. Zare Rameshti, S. Viola Kusminskiy, J. A. Haigh, K. Usami, D. Lachance-Quirion, Y. Nakamura, C.-M. Hu, H. X. Tang, G. E. Bauer, and Y. M. Blanter, Cavity magnonics, Phys. Rep. **979**, 1 (2022).

[5] Ö. O. Soykal and M. E. Flatté, Strong field interactions between a nanomagnet and a photonic cavity, Phys. Rev. Lett. **104**, 077202 (2010).

[6] H. Huebl, C. W. Zollitsch, J. Lotze, F. Hocke, M. Greifenstein, A. Marx, R. Gross, and S. T. B. Goennenwein, High cooperativity in coupled microwave resonator ferrimagnetic insulator hybrids, Phys. Rev. Lett. **111**, 127003 (2013).

[7] Y. Tabuchi, S. Ishino, T. Ishikawa, R. Yamazaki, K. Usami, and Y. Nakamura, High cooperativity in coupled microwave resonator ferrimagnetic insulator hybrids, Phys. Rev. Lett. **113**, 083603 (2014).

[8] X. Zhang, C.-L. Zou, L. Jiang, and H. X. Tang, Strongly coupled magnons and cavity microwave photons, Phys. Rev. Lett. **113**, 156401 (2014).

[9] M. Goryachev, W. G. Farr, D. L. Creedon, Y. Fan, M. Kostylev, and M. E. Tobar, High-cooperativity cavity QED with magnons at microwave frequencies, Phys. Rev. Appl. **2**, 054002 (2014).

[10] L. Bai, M. Harder, Y. P. Chen, X. Fan, J. Q. Xiao, and C.-M. Hu, Spin pumping in electrodynamically coupled magnon-photon systems, Phys. Rev. Lett. **114**, 227201 (2015).

[11] Justin T. Hou and Luqiao Liu, Strong coupling between microwave photons and nanomagnet magnons, Phys. Rev. Lett. **123**, 107702 (2019).

[12] Y. Li, T. Polakovic, Y.-L. Wang, J. Xu, S. Lendinez, Z. Zhang, J. Ding, T. Khaire, H. Saglam, R. Divan, J. Pearson, W.-K. Kwok, Z. Xiao, V. Novosad, A. Hoffmann, and W. Zhang, Strong coupling between magnons and microwave photons in on-chip ferromagnet-superconductor thin-film devices, Phys. Rev. Lett. **123**, 107701 (2019).

[13] Y. Tabuchi, S. Ishino, A. Noguchi, T. Ishikawa, R. Yamazaki, K. Usami, and Y. Nakamura, Coherent coupling between a ferromagnetic magnon and a superconducting qubit, Science **349**, 405 (2015).

[14] D. Lachance-Quirion, Y. Tabuchi, S. Ishino, A. Noguchi, T. Ishikawa, R. Yamazaki, and Y. Nakamura, Resolving quanta of collective spin excitations in a millimeter-sized ferromagnet, Sci. Adv. **3**, e1603150 (2017).

[15] X. Zhang, C.-L. Zou, N. Zhu, F. Marquardt, L. Jiang, and H. X. Tang, Magnon dark modes and gradient memory, Nat. Commun. **6**, 8914 (2015).

[16] R.-C. Shen, Y.-P. Wang, J. Li, S.-Y. Zhu, G. S. Agarwal, and J. Q. You, Long-time memory and ternary logic gate using a multistable cavity magnonic system, Phys. Rev. Lett. **127**, 183202 (2021).

[17] Y.-P. Wang, G.-Q. Zhang, D. Zhang, T.-F. Li, C.-M. Hu, and J. Q. You, Bistability of cavity magnon polaritons, Phys. Rev. Lett. **120**, 057202 (2018).

[18] D. Zhang, X.-Q. Luo, Y.-P. Wang, T.-F. Li, and J. Q. You, Observation of the exceptional point in cavity magnon-polaritons, Nat. Commun. **8**, 1368 (2017).

[19] G.-Q. Zhang, Z. Chen, D. Xu, N. Shammah, M. Liao, T.-F. Li, L. Tong, S.-Y. Zhu, F. Nori, and J. Q. You, Exceptional point and cross-relaxation effect in a hybrid quantum system, PRX Quantum **2**, 020307 (2021).

[20] M. Harder, Y. Yang, B. M. Yao, C. H. Yu, J. W. Rao, Y. S. Gui, R. L. Stamps, and C.-M. Hu, Level attraction due to dissipative magnon-photon coupling, Phys. Rev. Lett. **121**, 137203 (2018).

[21] B. Bhoi, B. Kim, S.-H. Jang, J. Kim, J. Yang, Y.-J. Cho, and S.-K. Kim, Abnormal anticrossing effect in photon-magnon coupling, Phys. Rev. B **99**, 134426 (2019).

[22] Y.-P. Wang, J. W. Rao, Y. Yang, P.-C. Xu, Y. S. Gui, B. M. Yao, J. Q. You, and C.-M. Hu, Nonreciprocity and unidirectional invisibility in cavity magnonics, Phys. Rev. Lett. **123**, 127202 (2019).

[23] Y. Yang, Y.-P. Wang, J. W. Rao, Y. S. Gui, B. M. Yao, W. Lu, and C.-M. Hu, Unconventional singularity in anti-parity-time symmetric cavity magnonics, Phys. Rev. Lett. **125**, 147202 (2020).

[24] J. Xu, C. Zhong, X. Han, D. Jin, L. Jiang, and X. Zhang, Floquet cavity electromagnonics, Phys. Rev. Lett. **125**, 237201 (2020).

[25] H. Deng, H. Haug, and Y. Yamamoto, Exciton-polariton Bose-Einstein condensation, Rev. Mod. Phys. **82**, 1489 (2010).

[26] M. Harder, B. M. Yao, Y. S. Gui, and C.-M. Hu, Coherent and dissipative cavity magnonics, J. Appl. Phys. **129**, 201101 (2021).

[27] Bimu Yao, Y. S. Gui, J. W. Rao, Y. H. Zhang, W. Lu, and C.-M. Hu, Coherent microwave emission of gain-driven polaritons, Phys. Rev. Lett. **130**, 146702 (2023).

[28] H. L. Stover and W. H. Steier, Locking of laser oscillators by light injection, Appl. Phys. Lett. **8**, 91 (1966).

[29] Y.-Y. Liu, J. Stehlik, M. J. Gullans, J. M. Taylor, and J. R. Petta, Injection locking of a semiconductor double-quantum-dot micromaser, Phys. Rev. A **92**, 053802 (2015).

[30] M. C. Cassidy, A. Bruno, S. Rubbert, M. Irfan, J. Kammhuber, R. N. Schouten, A. R. Akhmerov, and L. P. Kouwenhoven, Demonstration of an ac Josephson junction laser, Science **355**, 939 (2017).

[31] L. Gilles and P. L. Knight, Two-photon absorption and nonclassical states of light, Phys. Rev. A **48**, 1582 (1993).

[32] T. E. Lee and H. R. Sadeghpour, Quantum synchronization of quantum van der Pol oscillators with trapped ions, Phys. Rev. Lett. **111**, 234101 (2013).

[33] B. van der Pol, A theory of the amplitude of free and forced triode vibrations, Radio Rev. **1**, 701 (1920).

[34] E. G. Spencer, R. C. LeCraw, and R. C. Linares, Low-temperature ferromagnetic relaxation in yttrium iron garnet, Phys. Rev. **123**, 1937 (1961).

[35] V. I. Arnold, *Mathematical Methods of Classical Mechanics* (Springer-Verlag, Berlin, 1974).

[36] A. Pikovsky, M. Rosenblum, and J. Kurths, *Synchronization: A Universal Concept in Nonlinear Sciences* (Cambridge University Press, Cambridge, U.K., 2001).

[37] S. H. Strogatz, *Nonlinear Dynamics and Chaos: with Applications to Physics, Biology, Chemistry, and Engineering* (CRC Press, Boca Raton, 2018).